The Spatial Resolution Enhancement for a Thermogram Enabled by Controlled Subpixel Movements

Weixiang Du, Sri Addepalli, and Yifan Zhao

Abstract—The measurement accuracy and reliability of thermography are largely limited by a relatively low spatial resolution of the thermal imager. Using a high-end camera to achieve high spatial resolution can be expensive or infeasible as a high sample rate is required. Furthermore, system miniaturization becomes an inevitable trend with the continuous development of the Internet of Things (IoT) and their suitability to *in situ* inspection scenarios. However, a miniaturized sensor usually suffers from low spatial resolution. Addressing this challenge, this article reports a novel spatial resolution enhancement for a thermogram (SRE4T) system to significantly improve the spatial resolution without upgrading the sensor. A high-resolution (HR) thermal image is reconstructed by fusing a sequence of low-resolution (LR) images with subpixel movements. To achieve the best image quality, instead of benefiting from natural movements of the existing studies, this article proposes to use an HR xy translation stage to produce a sequence of controlled subpixel movements. The performance of the proposed system was tested on both high-end and low-end thermal imagers. Both visual and quantitative results successfully demonstrated the considerable improvement of the quality of thermal images [up to 30.5% improvement of the peak signal-to-noise ratio (PSNR)]. This technique allows improving the measurement accuracy of thermography inspection without upgrading sensors. It also has potential to be applied on other imaging systems.

Index Terms—Image reconstruction, motion estimation, NDT, resolution enhancement.

I. INTRODUCTION

INFRARED (IR) thermography is a noncontact nondestructive testing (NDT) method and offers a robust and rapid platform for inspection while covering a large area within a short time frame, and thus it is potentially adaptable to in-service monitoring applications [1], [2] for electrical equipment [3], [4], mechanical equipment [5], welding [6], and structural [7], [8], and aerospace composite materials [9]. However, in comparison with other NDT methods such as X-ray and ultrasound, thermography has a relatively low

spatial resolution (typically 640×480 pixels). Although some latest thermal imaging technologies have been achieved [10], the spatial resolution is still the major limiting factor and bottleneck for industrial applications of thermography [11], mainly due to the refinement needed for improved anomaly feature extraction. A high-end IR camera with a high spatial resolution is usually costly, which is driven by the use of quantum detectors, e.g., mercury cadmium telluride, indium antimonide, etc. Additionally, the maximum spatial resolution may be unachievable when a high sample rate has to be used for materials such as metals and alloys as they have high thermal-conductivity. Furthermore, even with the same spatial resolution, the boundary of objects or discontinuity in thermal images is not as sharp as that of digital images. This is related to their imaging principles [12]–[14]: the digital imaging system normally acquires images using CCD/CMOS sensors, which is based on the difference in the intensity of light in the range of 0.4–0.7 μm reflected by the surface of the observed target, with a high contrast and improved resolution. IR thermal imaging technology is based on receiving radiant energy with longer wavelengths in the range of 3–12 μm. Due to the influence of atmospheric conditions, the difference in minimum resolvable temperature difference between the object and the background together with the distance it is measured from, the target is easily submerged in the dark background, which leads to the blurring effect of the acquired thermal image. The existing low-cost IR cameras usually have disadvantages such as low contrast, edge blurring, large noise, low clarity, and poor ability, which make it difficult to define the boundary and accurately measure the shape of targets. There is a strong demand to improve the quality of thermal images without upgrading hardware in the context of NDT and surveillance systems.

With the increase of functionality integration, the complexity of industrial products and increasing use of advanced materials into complex systems, the heavy weight and large size of equipment has become the bottleneck to deploy NDT devices in *in situ* inspection. Developing lightweight and miniaturized NDT equipment to inspect various materials for the degradation assessment of inaccessible area becomes more and more important [15]. Furthermore, the serviceability of components or systems to be inspected has now become challenging, particularly in determining their maintenance requirements, as disassembly and inspection are very expensive. The trend is now in the development of portable equipment that will improve the maintenance and performance of the system that

is being monitored. The rapid development of the Internet of Things (IoT) technology has promoted the development of small sensors which contained the feature of small size and low power consumption [16]. However, it brings some problems such as poor image quality, low resolution (LR), and sensitivity in addition to the ability to transfer large data sets wirelessly.

There are a few studies reported to improve the quality of thermal images, and are largely based on single image enhancement or super-resolution (SR). The key of SR is to capture multiple subpixel LR images at pre-defined locations for the same scene and rebuild the high-resolution (HR) images by integrating these images and restoring the missing signals into one pixel, which greatly improves the image quality. In the category of single image enhancement, Holland and Renshaw [17] proposed a physics-based method that used the basic principles of the physics of thermal diffusion to improve the spatial resolution of the thermogram. Another attempt was done by Ashiba *et al.* [18] who presented a new approach based on contrast limited adaptive histogram equalization to improve the IR images. In the category of SR, Alam *et al.* [19] proposed a gradient-based registration algorithm to estimate the shifts between the acquired thermal images and then used a weighted nearest-neighbor approach for placing the frames onto a uniform grid to form a final HR image. The quality of the produced HR image relies on how well the subpixel motions are uniformly distributed. However, the shifts were caused by the vibrations from the platform on which the camera was mounted, which is uncontrollable and random, such as a commercial tool FLIR UltraMax [20], and Sadi and Crastes [21]used an uncooled microbolometer array to produce an HR thermal imaging by taking advantages of the relative motion between the camera and the object to produce information redundancy. Kaczmarek and Borwanski [22] used recording time series of thermograms to reconstruct a thermal image with improved spatial resolution. Mwangi *et al.* [23] proposed a fusion of active thermography and visible imagery data, capable of producing higher resolution thermograms based on the physical boundaries in the visible domain. The sharpness of the thermogram was improved based on the additional information obtained from the digital image. Collectively, SR-based approaches usually produce better results than the single image enhancement methods, because they increase the entropy of the images through benefiting from the true measurements of multiple images. Single image enhancement methods either improve the visualization, while no extra information is introduced, or apply the physics knowledge to reduce the blurring but the model to be applied is quite subjective.

To the best of authors' knowledge, most of the existing SR-based approaches employed to improve the quality of thermal images focus on how to reconstruct the HR image based on the captured LR images, where the movements are natural and uncontrollable, and therefore the image quality is not guaranteed. Very few studies investigate how to produce the LR images to achieve the best performance of resolution improvement. This article reports a novel spatial resolution enhancement for a thermogram (SRE4T)
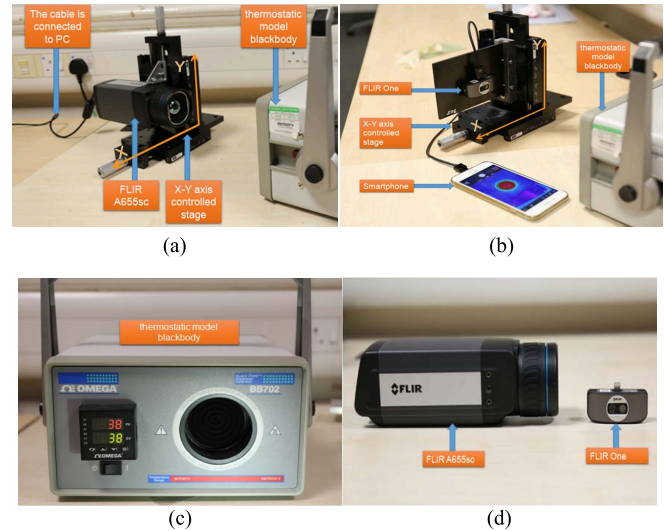

Fig. 1. Experimental setup. (a) Experimental setup for FLIR A655sc. (b) Experimental setup for FLIR ONE. (c) IR blackbody calibrator (OMEGA BB702). (d) FLIR A655sc and FLIR ONE cameras.

system, first time to propose to maximize and guarantee the performance of resolution improvement benefiting from accurately controlled subpixel movements. This technique contributes to the improvement of the measurement accuracy of thermographic inspection and the reduction of uncertainty of defect/damage detection. The system includes the experimental setup, image reconstruction, and performance evaluation.

II. METHODS

A. Experimental Setup

To capture a sequence of raw thermal images with subpixel shifts in both x- and y-direction, an experimental setup is introduced and illustrated in Fig. 1(a) and (b). A thermal camera is mounted on a high accuracy x-y translation stage with a resolution of ± 1 μm. An IR blackbody calibrator (OMEGA BB702), as illustrated in Fig. 1(c), is used as the observed object. The 2.5-in (63.5 mm) diameter target plate has an emissivity of 0.95 and can be set to a range of temperatures between ambient $+32\,°C$ and $–215\,°C$. To ensure the observed object has the exact same temperature distribution during the data acquisition of multiple images, the temperature of the calibrator was fixed at 38 °C with the room reflected temperature recorded at 22 °C and with a relative humidity value of 55%.

There are two potential motion modes: one is the object moves and the camera is fixed, and the other is the object is fixed while the camera moves. Both modes can introduce a global subpixel motion, which is a key to increase the resolution of static objects. In this article, the latter mode is employed. The main reason for this setup was due to the heavyweight of the blackbody calibrator and the relatively low weight of cameras (as seen in Fig. 1).

To create the subpixel movements required for the SR technique, for each data capture, the translation stage moves a step of $1/a$ pixel either in the x- or y-direction, where a

($a > 1$) is the scale factor to achieve. Assuming the object position in the thermal image on the first data capture as the reference, denoted (x_0, y_0), the camera is moved to ensure that the following positions of the object on the thermal image are achieved

$$(x_0, y_0), \left(x_0 + \frac{1}{a}, y_0\right), \ldots, \left(x_0 + \frac{a-1}{a}, y_0\right)$$
$$\left(x_0, y_0 + \frac{1}{a}\right), \left(x_0 + \frac{1}{a}, y_0 + \frac{1}{a}\right), \ldots, \left(x_0 + \frac{a-1}{a}, y_0 + \frac{1}{a}\right),$$
$$\vdots$$
$$\left(x_0, y_0 + \frac{a-1}{a}\right), \left(x_0 + \frac{1}{a}, y_0 + \frac{a-1}{a}\right), \ldots,$$
$$\left(x_0 + \frac{a-1}{a}, y_0 + \frac{a-1}{a}\right). \quad (1)$$

It can be inferred from (1) that the total number of images to be captured is a^2.

The movement step of the translation stage depends on the intrinsic parameters of the camera and the distance from the camera to the object surface. This article uses a simple calibration process to achieve a parameter α, which indicates the required millimeter movement of the stage in the x- or y-direction to achieve a representative shift of one-pixel in the thermal image. In this article, one thermal image was captured along the x-direction of the stage, which represents a shift of 1 mm. The shift of the calibrator on the thermal images is now measured and denoted as m pixels. Then, α is written as

$$\alpha = 1/m. \quad (2)$$

This step can then be repeated for the y-direction. To simplify the process, this article uses the same value of α for both the x- and y-directions.

In this article, two thermal cameras have been tested, as shown in Fig. 1(d). The FLIR A655sc, a high-end IR camera with a resolution of 640×480 pixels, was used to demonstrate the proof of concept. Quantitative evaluation of the performance is conducted with this camera, as it can offer an HR reference image. Resolution enhancement of this camera could lead to the improvement of detection accuracy and reliability. A low-end miniature IR camera, the FLIR ONE with a resolution of 160×120 pixels, was then used to validate the proposed technique for a miniaturized sensor where the imaging quality is compromised for portability. This case study aims to explore the potential of SRE4T in *in situ* inspection scenarios. The key parameters of the two cameras are shown in Table I. Both cameras have a similar spectral range, but have a huge difference in spatial resolution, size, and weight.

The distance between the camera and the calibrator surface was adjusted to ensure a good field of view of the calibrator. For the FLIR A655sc, the distance was set as 300 mm, and the estimated α is 20 μm. Considering the minimal step of the stage (1 μm), 20 movements should be conducted in each direction to achieve one-pixel movement in images. Therefore, theoretically, the maximal achievable scale factor of resolution for this setting is 20. For the FLIR ONE, the distance was set as 140 mm to ensure a similar field of

TABLE I
SPECIFICATION OF THE TESTED TWO CAMERAS

Specification	FLIR A655sc	FLIR one
Spectral range	7.5 – 14.0 μm	8 – 14 μm
Resolution	640 x 480	160 x 120
Focus	24.6 mm - Infinity	150 mm - Infinity
Pixel size	17 μm	12 μm
Frame rate	50 Hz	8.7Hz
Accuracy	±2°C or ±2% of Reading	±3°C or ±5% of Reading Percent of the difference between ambient and scene temperature.
Measurement temperature	–40°C to 150°C	-20°C - 120°C
Operating temperature	-15°C to 50°C	0°C – 35°C
Size	216 × 73 × 75 mm	65x29x18mm
Weight	900g	32g

view (the FLIR ONE has a wider angle of the lens) as the FLIR A655sc, and the estimated α is 40 μm. The maximal achievable scale factor of resolution in the latter case is 40. It should be noted that the achievable maximal scale factor depends on the working distance, focus, stage step, and camera specifications.

B. Superresolution Algorithm

There are two main stages to fuse the captured LR raw images into an HR image: the image registration and the image construction. Image registration aims at the estimation of motion parameters between the LR images, while image reconstruction aims at combining the registered LR image to reconstruct an HR image by using the estimated motion parameters. It should be noted that the image registration step can be skipped if the motions are perfectly controlled. For this article, this step was still implemented since the motion was controlled manually and has limited accuracy.

1) Image Registration: Image registration methods can be operated either in the spatial-domain or the frequency-domain. Frequency-domain methods are usually limited to global motion models, whereas spatial-domain methods usually allow more general motion models. In this article, the method developed by Keren et al. [24] was employed to estimate the shifts (both horizontal and vertical shifts) and rotations among the LR images due to its fine performance to tackle the global motion.

The relation between the horizontal shift a, the vertical shift b, and the rotation angle θ between the LR images f and g can be written as

$$g(x, y) = f(x \cos(\theta) - y \sin(\theta) + a,$$
$$y \cos(\theta) + x \sin(\theta) + b). \quad (3)$$

Expanding $\sin(\theta)$ and $\cos(\theta)$ to the first two terms in their Taylors series expansion gives the following equation:

$$g(x, y) \approx f(x + a - y\theta - x\theta^2/2, y + b + x\theta - y\theta^2/2). \quad (4)$$

Expanding f to the first term in its Taylors series gives the first-order equation

$$g(x, y) \approx f(x, y) + (a - y\theta - x\theta^2/2)\frac{\partial f}{\partial x}$$
$$+ (b + x\theta - y\theta^2/2)\frac{\partial f}{\partial y}. \quad (5)$$

The error between g and f after translation by a and b and rotation by θ, expressed as E, can thus be approximated as

$$E(a, b, \theta) = \sum \left[f(x, y) + (a - y\theta - x\theta^2/2)\frac{\partial f}{\partial x} \right.$$
$$\left. + (b + x\theta - y\theta^2/2)\frac{\partial f}{\partial y} - g(x, y) \right]^2 \quad (6)$$

where the summation is over the overlapping area of f and g.

The minimum of $E(a, b, \theta)$ can be obtained by computing its derivatives with respect to a, b, and θ and setting them to zero. The difference between g and f warped by (a, b, θ) will be minimized by solving the following equation for a, b, and θ:

$$\left[\sum \left(\frac{\partial f}{\partial x}\right)^2 \right] a + \left[\sum \frac{\partial f}{\partial x}\frac{\partial f}{\partial y} \right] b + \left[\sum R\frac{\partial f}{\partial x} \right] \theta$$
$$= \sum \frac{\partial f}{\partial x}(f - g)$$

$$\left[\sum \frac{\partial f}{\partial x}\frac{\partial f}{\partial y} \right] a + \left[\sum \left(\frac{\partial f}{\partial y}\right)^2 \right] b + \left[\sum R\frac{\partial f}{\partial y} \right] \theta$$
$$= \sum \frac{\partial f}{\partial y}(f - g)$$

$$\left[\sum R\frac{\partial f}{\partial x} \right] a + \left[\sum R\frac{\partial f}{\partial y} \right] b + \left[\sum R^2 \right] \theta$$
$$= \sum R(f - g) \quad (7)$$

where $R = x(\partial f/\partial y) - y(\partial f/\partial x)$.

By solving this set of linear equations, the motion parameters a, b, and θ can then be computed.

2) Image Reconstruction: Pham et al. [25] proposed the so-called structure-adaptive normalized convolution (SANC) reconstruction method for the fusion of irregularly sampled data obtained from different LR images. The method is based on the normalized convolution (NC) method [26], which approximates the local signal from projections onto a set of polynomial basis functions. Employing the polynomial basis functions in the NC makes it equal to a local Taylor series expansion. Considering a local neighborhood centered at $s_0 = \{x_0, y_0\}$, the intensity value at position $s = \{x, y\}$ in the HR image is estimated using a polynomial expansion written as

$$\hat{f}(s, s_0) = P_0(s_0) + P_1(s_0)x + P_2(s_0)y + P_3(s_0)x^2$$
$$+ P_4(s_0)xy + P_5(s_0)y^2 + \cdots \quad (8)$$

where

$$x = \alpha \cos(\theta)(a + x_0) - \alpha \sin(\theta)(b + y_0) \quad (9)$$
$$y = \alpha \sin(\theta)(a + x_0) + \alpha \cos(\theta)(b + y_0). \quad (10)$$

$P(s_0) = [P_0 P_1 \dots P_m]^T(s_0)$ are the projection coefficients their entire polynomial basis functions at s_0.

A structure-adaptive applicability function is used in NC to localize a polynomial approximation, which gives different weights to all data points in a neighborhood in the image. In addition, the signal certainty is introduced in NC to ensure each input signal due to its certainty value and reduce the impact of outliers caused by missing samples or erroneous registration.

C. Performance Evaluation

This section presents the approach to quantify the resolution improvement of the proposed system. The peak signal-to-noise ratio (PSNR) between the super-resolved image and the original HR image is one of the most commonly used objective fidelity criteria for evaluating image quality. It can be calculated as

$$\text{PSNR} = 10 \log_{10}\left(\frac{L^2}{\text{MSE}}\right) \quad (11)$$

where L is the maximum fluctuation in the image. The higher the PSNR, the better the improvement is. If the image is represented by an 8-bit grayscale, the value of L will be 255. MSE represents the mean-square-error between the super-resolved image $\hat{X}(i, j)$ and the original HR image $X(i, j)$. It can be calculated as

$$\text{MSE} = \frac{1}{W \times H} \sum_{i=1}^{W}\sum_{j=1}^{H}[\hat{X}(i, j) - X(i, j)]^2 \quad (12)$$

where W and H denote the width and the height of the image.

Entropy is another quantitative measure used to assess image quality when the error images for different image resolution enhancement techniques are very close to each other and it is very difficult to make a firm assessment. The entropy of a negative error image, denoted ET, can be calculated as

$$\text{ET} = -\sum_{k=1}^{L} P(r_k)\log_2 P(r_k) \quad (13)$$

where $P(r_k)$ is the probability of an intensity value r_k. The lower the ET, the better the improvement is [27].

To complement the quantitative analysis, the structural similarity (SSIM) [28] image quality measure has also been applied. The SSIM index evaluates the visual effect of three characteristics of an image: luminance, contrast, and structure. It is based on the computation of these three components and is an inner product of them. It is defined as

$$\text{SSIM} = \frac{(2\mu_{\hat{X}}\mu_X + C_1)(2\sigma_{\hat{X}}\sigma_X + C_2)}{(\mu_{\hat{X}}^2 + \mu_X^2 + C_1)(\sigma_{\hat{X}}^2 + \sigma_X^2 + C_2)} \quad (14)$$

where $\mu_{\hat{X}}, \mu_X$ are the local means for the images $\hat{X}$ and X, respectively; $\sigma_{\hat{X}}, \sigma_X$ are the corresponding standard deviations; and C_1, C_2 are two constants used to avoid the instability. The higher the SSIM, the better the improvement is.

D. Experiment Plan

To evaluate the performance of resolution improvement qualitatively and quantitatively, three experiments were conducted.

Experiment 1: FLIR A655sc was used and α was chosen as 20 μm. Three groups of data were collected aiming to achieve the scale factors of 2, 3, and 4, respectively. The resolution of the produced HR images is now at 1280×960, 1920×1440, and 2560×1920, respectively. A visual comparison (qualitative evaluation) was conducted between the produced HR images and the raw images with a resolution of 640×480. No quantitative evaluation was conducted for this experiment due to the lack of the reference image.

Experiment 2: FLIR ONE was used and α was chosen as 40 μm. Three groups of data were collected to achieve the scale factors of 2, 3, and 4, respectively. The resolution of the produced HR images is 320×240, 480×360, and 640×480, respectively. A visual comparison was conducted between the produced HR images and the raw images with a resolution of 160×120. No quantitative evaluation was conducted for this experiment due to the lack of the reference image.

Experiment 3: FLIR A655sc was used and α was chosen as $20a$ μm, where a is the scale factor. The captured raw images $\text{IMR}_i (i = 1, 2, \ldots, a^2)$ with a resolution of 640×480 were downsized to $640/a$ by $480/a$, denoted IML_i $(i = 1, 2, \ldots, a^2)$. The SR technique was then applied on these LR images to reconstruct an HR image with a resolution of 640×480, denoted IMH. IMR_i now becomes the reference HR image, which allows a quantitative evaluation on the similarity between IMH and IMR_i. Three criteria were calculated to represent the quality improvement, and can be written as

$$\text{m\_PSNR} = \max_i \text{PSNR}(\text{IMR}_i, \text{IMH}) \qquad (15)$$

$$\text{m\_SSIM} = \max_i \text{SSIM}(\text{IMR}_i, \text{IMH}) \qquad (16)$$

and

$$\text{m\_ET} = \max_i \text{ET}(\text{IMR}_i, \text{IMH}). \qquad (17)$$

Three scale factors of 2, 3, and 4 were tested.

III. RESULTS

A. Experiment 1

Fig. 2 shows a snapshot of the captured thermal image using FLIR A655sc with a spatial resolution of 640×480 pixels. As shown in Fig. 1(c), the blackbody calibrator is an off-the-shelf unit with a ridged hot plate. The ridges are clearly seen in Fig. 2. In typical calibration measurements, having a flat hot plate may not be efficient as the data may be influenced by the angle of measurement and often needs to be compared with multiple sources. Having concentric ridges allows the global average of the temperature and provides a more accurate measure of the temperature.

A total number of 4, 9, and 16 images with this resolution were captured for the scale factors of 2, 3, and 4, respectively. To better demonstrate the details of improvement, six regions of interest with the size of 20×20 pixels, as highlighted
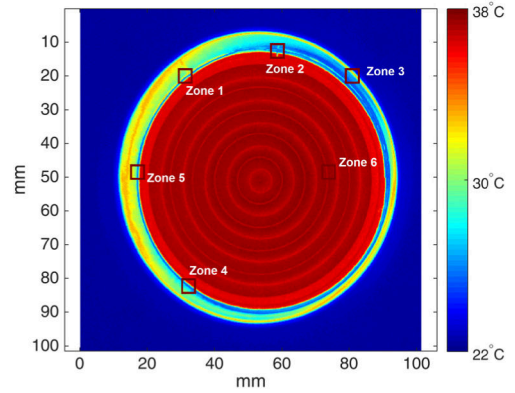

Fig. 2. Representative thermal image of the blackbody calibrator acquired using FLIR A655sc, where the temperature was set as 38 °C and the room temperature is 22 °C. The regions of interest for resolution improvement are highlighted by rectangles.
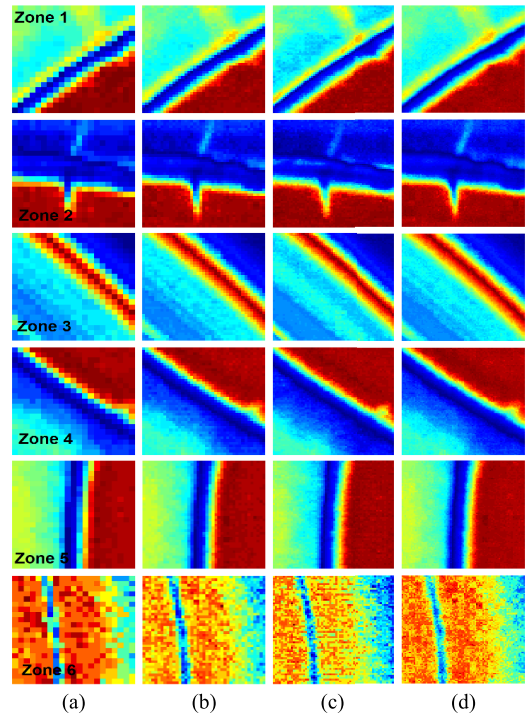

Fig. 3. Comparison of superresolved HR image from passive thermography using FLIR A655sc. The selected regions are highlighted in Fig. 2 from zones 1 to 6, respectively. It should be noted that the colormap could be different from Fig. 2 for better visualization. (a) Raw image. (b) 2×. (c) 3×. (d) 4×.

in Fig. 2, are compared between the raw image and the super-resolved images in Fig. 3. Zones 1–5 show the performance on high contrast areas, while zone 6 shows the performance on a relatively low contrast area. It can be clearly observed that the proposed SRE4T technique significantly improved the sharpness of both high and low contrast boundaries and is evidenced by reduced pixilation and improved sharpness of the image. With the increment of the scale factor, more and more details have been recovered in the HR images. The selected zones also include different directions of the boundary, including 0° (zone 2), 45° (zones 1, 3, and 4), and 90° (zones 5 and 6). The results demonstrate that this

Fig. 4.   Snapshot of the observed "v" shape feature (red circled) shown in zone 2.
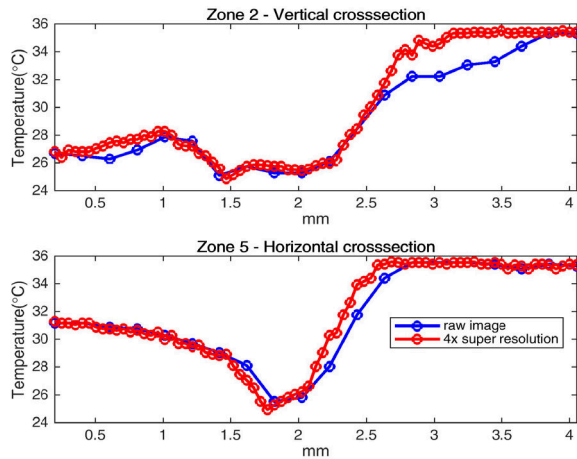

Fig. 5.   1-D plot comparison between the raw LR image and the 4× SR image using FLIR A655sc.

system can improve the spatial resolution in all the observed directions. In zone 2, the "v" shape feature is presented in a much clearer manner using the scale factor of 4, in comparison with the raw captured image. Fig. 4 shows a digital image of zone 2, where the small feature can be clearly observed. This level of improvement is unlikely to be achieved using the traditional interpolation-based approach.

To explore more details of improvement, a vertical cross section in the middle of the image for zone 2 and a horizontal cross section for zone 5 are shown in Fig. 5 to compare the difference between the raw image (denoted by the blue curve) and the HR image (denoted by the red curve) with the scale factor of 4. It can be clearly observed that the red curve has a higher slope than the blue curve between the regions of 2 and 3 mm along the x-axis. This observation suggests that the produced HR image is a better representation of the ground truth, where the blackbody has a sharp temperature change in that region.

It should be noted that the performance of the introduced technique highly depends on the accuracy of the motions. Fig. 6 shows the comparison between the estimated motions (blue dots) using the employed image registration method and the ideal motions (red dots) for the three scale factors. The absolute errors of both directions are shown in Table II. It suggests that: 1) the error is smaller than 0.03 pixels for

TABLE II
ABSOLUTE ERRORS OF MOTIONS FOR FLIR A655SC

Scale factor	X axis (pixel)	Y axis (pixel)
2	0.0099±0.0097	0.0215±0.0191
3	0.0127±0.0123	0.0220±0.0159
4	0.0240±0.0207	0.0294±0.0172

both directions; 2) the error in the y-axis is higher than that in the x-axis which may be due to the stage layout or the fact that α was calibrated in the x-direction only; and 3) the error increases following the increment of the scale factor, which is potentially caused by human error due to the reduced movement step of the stage. The observation 3) also indicates that the maximum scale factor may be not achievable due to the increased error of motion following the increment of the scale factor.

B. Experiment 2

Fig. 7 shows a snapshot of the captured thermal image using FLIR ONE with a spatial resolution of 160×120 pixels. In comparison to Fig. 2, the poor, degraded quality of the image can be clearly observed. In line with the lower pixel resolution, a wider angle of the lens, a miniature sensor size, and a large stand-off distance clearly contribute to the image quality. Furthermore, the image shows a great deal of pixilation even at the full field of view even before reviewing the highlighted zones of interest. Super-resolved results of the highlighted six regions of interest with the size of 5×5 pixels (to ensure the same spatial size as experiment 1) are shown in Fig. 8. It can be observed that the image sharpness on boundaries has a large improvement in each direction. The image quality becomes better and better following the increment of the scale factor. However, the level of improvement is not as significant as that of experiment 1, even though the motions applied are very close to the ideal values, as shown in Fig. 9.

C. Experiment 3

This section aims to quantify the quality improvement using the proposed technique. The well-accepted nearest neighbor and the bicubic interpolation method are selected as the baseline. Each IML_i was applied by these interpolation methods and compared with IMR_i to calculate the PNSR, SSIM, and entropy for each pair. The maximum of PNSR and SSIM and the minimum of entropy were then calculated, based on (15)–(17), to represent the improvement of the interpolation methods.

The comparison of calculated criteria for two interpolation methods and the proposed technique is shown in Table III. Taking the m_PSNR values for example, it can be calculated that the proposed method produced

$$(41.70 - 31.96)/31.96 = 30.5\% \qquad (18)$$

$$(40.65 - 31.32)/31.32 = 29.8\% \qquad (19)$$

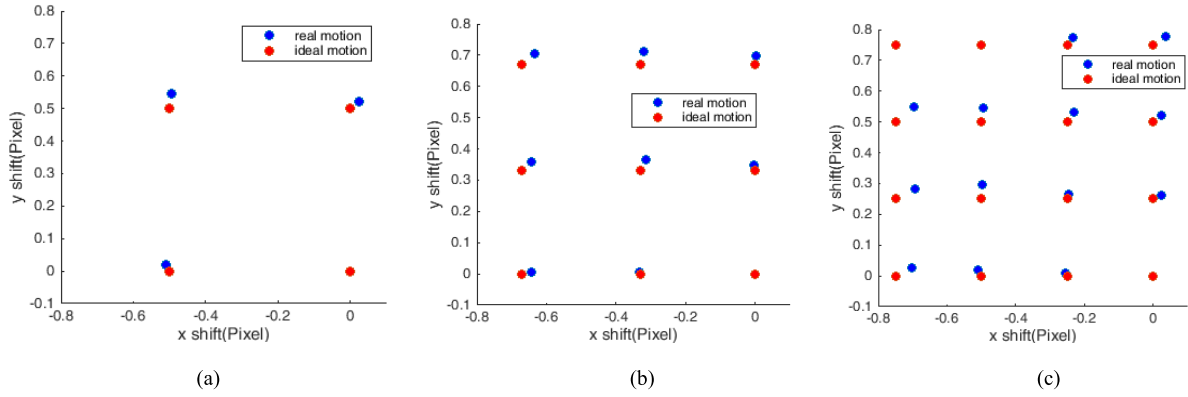$$(35.36 - 28.60)/28.60 = 23.6\% \qquad (20)$$

Fig. 6. Measured motion in the *x*- and *y*-directions for the thermal image using FLIR A655sc when the IR camera moves (blue dots), where the ideal motion parameters are also plotted (red dots). (a) 2×. (b) 3×. (c) 4×.
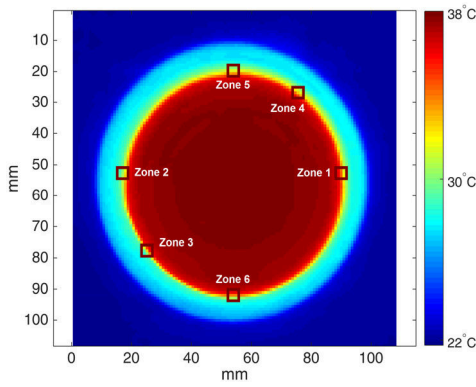

Fig. 7. Representative thermal image of the blackbody calibrator acquired using FLIR ONE, where the temperature was set to 38 °C and the room temperature is 22 °C. The regions of interest for resolution improvement are highlighted by rectangles.

TABLE III

QUANTITATIVE PERFORMANCE COMPARISON OF THE PROPOSED TECHNIQUE WITH CLASSIC INTERPOLATION METHODS FOR EXPERIMENT 3

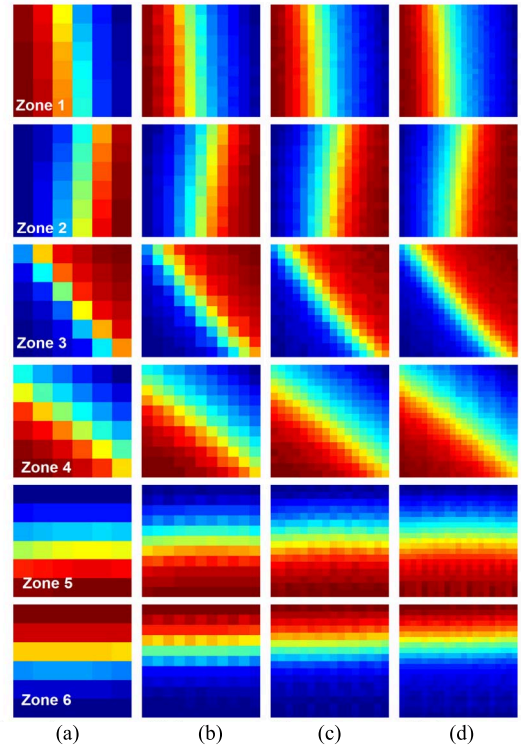|	Scale factor	Nearest interpolation	*Bicubic* interpolation	Proposed method
m_PSNR	2	31.96	34.27	**41.70**
	3	31.32	36.30	**40.65**
	4	28.60	32.12	**35.36**
m_SSIM	2	0.94	0.96	**0.97**
	3	0.93	0.96	**0.96**
	4	0.91	0.94	**0.95**
m_ET	2	3.54	2.39	**2.24**
	3	3.64	2.67	**2.47**
	4	3.56	2.80	**2.63**

Fig. 8. Comparison of the superresolved HR image from passive thermography using FLIR ONE. The selected regions are highlighted in Fig. 7 from zones 1 to 6, respectively. It should be noted that the colormap could be different from Fig. 7 for better visualization. (a) Raw image. (b) 2×. (c) 3×. (d) 4×.

increment against the nearest neighbor interpolation for the scale factors of 2, 3, and 4, respectively. In comparison with the most well-accepted bicubic interpolation, our method produced 21.7%, 11.9%, and 10.1% increment in percentage. Similar observations are applicable on m_SSIM and m_ET. The proposed method consistently produced the best results with a significant margin.

Fig. 10 shows the visual comparison between the raw HR image (640 × 480), the down-sampled LR image (160×120), the bicubic interpolated HR image (640 × 480), and the HR image (640 × 480) produced by the SRE4T system with the scale factor of 4. A region of 120 × 120 pixels of the HR image is shown to better visualize the difference. It can be clearly observed that the proposed method produced a much better recovery of the ground truth. While achieving the image close to the raw HR image would be an ideal case, the sensor currently does not come with that level of refinement in the real case, and is evidenced by the LR image. Though the
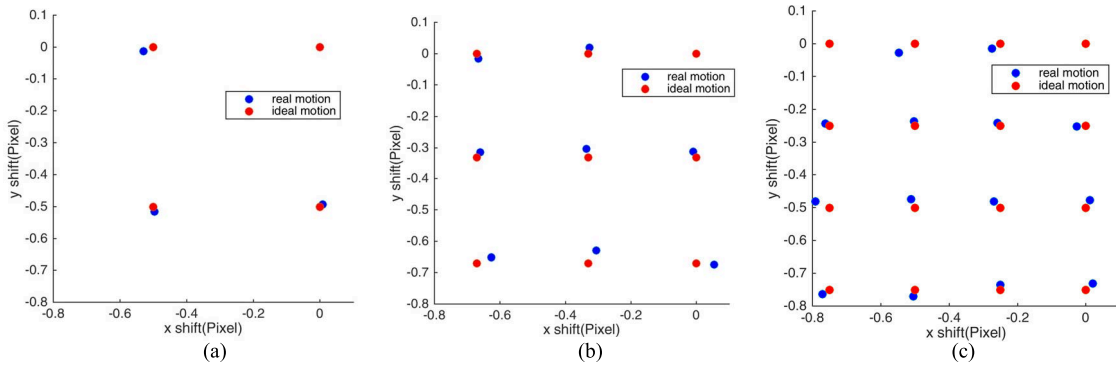
Fig. 9. Measured motion in the x- and y-directions for the thermal image using FLIR ONE when the IR camera moves (blue dots), where the ideal motion parameters are also plotted (red dots). (a) 2×. (b) 3×. (c) 4×.
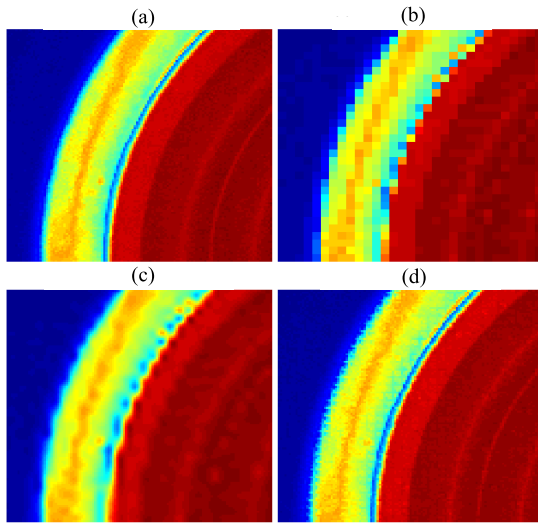

Fig. 10. Comparison of the (a) raw HR image, (b) resized LR image, (c) bicubic interpolated HR image, and (d) super-resolved HR image using the proposed technique for the scale factor of 4.

boundary of the bicubic interpolated image improved from the pixelated LR image, the image now includes a minor distortion combined with blurriness of the image boundary. The super-resolved image, however, shows significant improvement in comparison with the LR image. Furthermore, the sharpness of the image also seems to have improved and shows a better image in comparison with the bicubic interpolated image. The only minor downside is that the outer edge which is close to the reflected temperature of the room adds edge artifacts (boundary between the blue and yellow bands), whereas the high-temperature bands (represented by various shades of red) show a true similarity with the raw HR image indicating that the performance of the sensor above the reflected temperature could improve the overall quality of the object being investigated.

IV. DISCUSSION

A. Motion Mode

This article introduces a representative method that allows for global motions to be incorporated during data capture, where the IR camera was mounted onto the xy translation stage. The choice of using an appropriate method needs to be evaluated to achieve a controlled motion, which is critical to improve the image quality. For instance, the global motion should be achieved by considering if the camera can be mounted onto a suitable translation stage or the sample being tested. Additionally, an appropriate field of view must be chosen to ensure only the targeted object is shown in the scene, by selecting the region of interest, changing the lens, or adjusting the working distance.

B. Passive and Active Mode

It should be noted that this article focuses only on passive thermography where there is no excitation involved and the temperature distribution of the object does not change. The proposed SRE4T technique also has the potential to be applied on the pulsed flash thermography where the temperature of the object changes and the data are recorded as a function of time. One uncertainty introduced by the active mode, which could affect the performance, is the actual applied heat. The assumption of the SRE4T technique is that the thermal behavior of the object does not change for tests with different motions. It is difficult to control the heat source to ensure the heat applied on the object surface is exactly the same for multiple tests as the system is still analogous in nature. The second difficulty is that the images selected for registration and reconstruction must be extracted at the same timestamp. This can be challenging due to the limitation of the sample rate and the potential difference from the initial temperature.

C. Maximal Achievable Scale Factor

Theoretically, this value depends on the working distance, stage step, and camera specifications. The results in this article have shown that the accuracy of motion control becomes more and more challenging following the increment of the scale factor. It could be caused by the human error when operating the stage, or the physical limitation of the stage. One potential solution is to automate this process by using a motorized xy translation stage. The stage movement, data capture, and image reconstruction can be automatically implemented using an algorithm. The advantages are that: 1) motion error caused by human can be reduced and 2) the operating speed of this system will be much faster.

V. CONCLUSION

Aiming to advance thermography by improving its accuracy, reliability, and adaptability on in-service inspection, this article proposes a robust SRE4T system to improve spatial resolution benefiting from accurately controlled subpixel movements. Both quantitative and qualitative results, for a high-end IR camera and a low-end IR camera, showed that this solution can significantly improve the spatial resolution of the acquired thermal images at the expense of consuming more time during data collection and the extra cost of the translation stage that is usually much cheaper than upgrading to an HR IR camera.

It should be noted that the experiments of this article focus on passive thermography, where it is assumed that the thermal diffusion during data acquisition is saturated and that no external pulse or excitation has been used to alter the diffusion. The speed to capture data is therefore not important theoretically. However, for real applications, it is always suggested to maximize the sample rate through an automated fast-moving xy translation stage.

This technique will potentially be applied on active thermography to advance NDT, where the challenge is that significant thermal diffusion takes place during data capture. In particular, for high thermal-conductivity materials, such as metals and alloys, the thermal diffusion is quick and the sample rate must be fast enough to ensure there is no or very limited thermal diffusion in-between the captured LR images. Such a problem could be mitigated through automatically controlling a high-speed camera and a fast-moving stage, but the problem cannot be solved entirely. Therefore, this solution is more suitable to inspect low thermal-conductivity materials, such as CFRP. Another solution is conducting a multiple-inspection process with identical inspection parameters, except for shifting the relative position between the camera and the sample, and then registering and reconstructing the LR images from the same time-stamp.

The proposed solution is also straightforward to extend to digital imaging. The ultimate aim is to advance the capability of the existing sensor through enhanced signal and image processing, thus achieving improved information on the features that will help discriminating the part with added confidence. Features which were once invisible now become visible and the measurement accuracy is improved, which improves not only the overall performance but also our ability to make confident decisions based on the thermogram. Meanwhile, with the reduction of instrument cost, it is envisaged that this work will be adapted to both passive and active thermography and will encompass the multidisciplinary field of digital imaging.

REFERENCES

[1] V. P. Vavilov and D. D. Burleigh, "Review of pulsed thermal NDT: Physical principles, theory and data processing," *NDT E Int.*, vol. 73, pp. 28–52, Jul. 2015.

[2] K. Chatterjee and S. Tuli, "Image enhancement in transient lock-in thermography through time series reconstruction and spatial slope correction," *IEEE Trans. Instrum. Meas.*, vol. 61, no. 4, pp. 1079–1089, Apr. 2012.

[3] M. S. Jadin and S. Taib, "Recent progress in diagnosing the reliability of electrical equipment by using infrared thermography," *Infr. Phys. Technol.*, vol. 55, no. 4, pp. 236–245, 2012.

[4] L. Liu, L. Wang, C. Guo, H. Mei, and C. Zhao, "Detecting defects in porcelain postinsulator coated with room temperature vulcanized silicone rubber by pulsed thermography," *IEEE Trans. Instrum. Meas.*, vol. 68, no. 1, pp. 225–233, Jan. 2019.

[5] G. Singh, T. C. A. Kumar, and V. N. A. Naikan, "Fault diagnosis of induction motor cooling system using infrared thermography," in *Proc. IEEE 6th Int. Conf. Power Syst. (ICPS)*, Mar. 2016, pp. 1–4.

[6] X. Lu *et al.*, "Detection of micro solder balls using active thermography technology and κ-means algorithm," *IEEE Trans. Ind. Informat.*, vol. 14, no. 12, pp. 5620–5628, Dec. 2018.

[7] A. Foudazi, M. T. Ghasr, and K. M. Donnell, "Characterization of corroded reinforced steel bars by active microwave thermography," *IEEE Trans. Instrum. Meas.*, vol. 64, no. 9, pp. 2583–2585, Sep. 2015.

[8] A. Foudazi, A. Mirala, and M. T. Ghasr, "Active microwave thermography for nondestructive evaluation of surface cracks in metal structures," *IEEE Trans. Instrum. Meas.*, vol. 68, no. 2, pp. 576–585, Feb. 2019.

[9] L. Cheng and G. Y. Tian, "Transient thermal behavior of eddy-current pulsed thermography for nondestructive evaluation of composites," *IEEE Trans. Instrum. Meas.*, vol. 62, no. 5, pp. 1215–1222, May 2013.

[10] Infratec. *New Infrared Camera ImageIR 9300 Series*. Accessed: Dec. 1, 2018. [Online]. Available: https://www.infratec.co.uk/thermography/infrared-camera/imageir-9300/

[11] H. Zhang, R. Yang, Y. He, A. Foudazi, L. Cheng, and G. Tian, "A review of microwave thermography nondestructive testing and evaluation," *Sensors*, vol. 17, no. 5, p. 1123, 2017.

[12] M. Mancuso and S. Battiato, "An introduction to the digital still camera technology," *ST J. Syst. Res.*, vol. 2, no. 2, pp. 1–9, 2001.

[13] P. J. Withagen, F. C. A. Groen, and K. Schutte, "CCD color camera characterization for image measurements," *IEEE Trans. Instrum. Meas.*, vol. 56, no. 1, pp. 199–203, Feb. 2007.

[14] W. E. Erkonen, "Basic principles of non-contact temperature measurement," in *Radiology 101: The Basics and Fundamentals of Imaging*. Philadelphia, PA, USA: Lippincott Williams and Wilkins, 1998, pp. 3–7.

[15] W. Du, Y. Zhao, R. Roy, S. Addepalli, and L. Tinsley, "A review of miniaturised non-destructive testing technologies for *in-situ* inspections," *Procedia Manuf.*, vol. 16, pp. 16–23, Jan. 2018.

[16] J. Gubbi, R. Buyya, S. Marusic, and M. Palaniswami, "Internet of Things (IoT): A vision, architectural elements, and future directions," *Future Generat. Comput. Syst.*, vol. 29, no. 7, pp. 1645–1660, 2013.

[17] S. D. Holland and J. Renshaw, "Physics-based image enhancement for infrared thermography," *NDT E Int.*, vol. 43, no. 5, pp. 440–445, Jul. 2010.

[18] H. I. Ashiba, H. M. Mansour, M. F. El-Kordy, and H. M. Ahmed, "A new approach for contrast enhancement of infrared images based on contrast limited adaptive histogram equalization," *Appl. Math. Inf. Sci. Lett.*, vol. 3, no. 3, pp. 123–125, 2015.

[19] M. S. Alam, J. G. Bognar, R. C. Hardie, and B. J. Yasuda, "Infrared image registration and high-resolution reconstruction using multiple translationally shifted aliased video frames," *IEEE Trans. Instrum. Meas.*, vol. 49, no. 5, pp. 915–923, Oct. 2002.

[20] FLIR. *Flir UltraMax*. Accessed: Dec. 1, 2018. [Online]. Available: https://www.flir.co.uk/discover/rd-science/ultramax--the-ultimate-resolution/

[21] J. Sadi and A. Crastes, "High resolution images obtained with uncooled microbolometer," in *Proc. SPIE*, vol. 6941, Apr. 2008, Art. no. 694106. doi: 10.1117/12.782783.

[22] M. Kaczmarek and M. Borwanski, "Resolution enhancement of thermal images in active dynamic thermography sequences," in *Proc. 11th Int. Conf. Quant. InfraRed Thermography*, Sep. 2012, pp. 1–7.

[23] G. Mwangi, P. Fieguth, and C. S. Garbe, "Thermography spatial resolution enhancement by non-rigid registration with visible imagery," in *Proc. IEEE Int. Conf. Image Process. (ICIP)*, Sep. 2015, pp. 2542–2546.

[24] D. Keren, S. Peleg, and R. Brada, "Image sequence enhancement using sub-pixel displacements," in *Proc. Comput. Soc. Conf. Comput. Vis. Pattern Recognit.*, Jun. 1988, pp. 742–746.

[25] T. Q. Pham, L. J. van Vliet, and K. Schutte, "Robust fusion of irregularly sampled data using adaptive normalized convolution," *EURASIP J. Adv. Signal Process.*, vol. 2006, no. 1, Dec. 2006, Art. no. 083268. doi: 10.1155/ASP/2006/83268.

[26] H. Knutsson and C.-F. Westin, "Normalized and differential convolution," in *Proc. IEEE Conf. Comput. Vis. Pattern Recognit.*, Jun. 1993, pp. 515–523.

[27] S. Azam, F. T. Zohra, and M. M. Islam, "A state-of-the-art review on wavelet based image resolution enhancement techniques: Performance evaluation criteria and issues," *Int. J. Image, Graph. Signal Process.*, vol. 6, no. 9, p. 35, Aug. 2014.

[28] Z. Wang, A. C. Bovik, H. R. Sheikh, and E. P. Simoncelli, "Image quality assessment: From error visibility to structural similarity," *IEEE Trans. Image Process.*, vol. 13, no. 4, pp. 600–612, Apr. 2004.

Sri Addepalli received the B.Eng. degree in mechanical engineering from Anna University, Chennai, India, in 2005, the M.Phil. degree in materials technology from Swansea University, Swansea, U.K., in 2011, and the Ph.D. degree in engineering physics from the University of Wales Trinity Saint David, Carmarthen, U.K., in 2017, through the Prince of Wales Innovation Scholarship Award.

He was a CSWIP Level 1 Thermography Inspector and a Level 2 Ultrasonic Inspector achieved through TWI, Cambridge, U.K. He is currently a Research Fellow in degradation assessment with Cranfield University, Bedford, U.K. He is also a Chartered Engineer (C.Eng) with the Engineering Council U.K. and a Full Professional Member of the Institute of Mechanical Engineering (IMechE), London, U.K., and the Institute of Engineering Technology (MIET), London. His current research interests include passive and active thermography and material/component damage characterization with specific expertise in composite materials.

Weixiang Du received the M.Sc. degree in mechanical engineering from the University of Portsmouth, Portsmouth, U.K. He is currently pursuing the Ph.D. degree with the School of Aerospace, Transport and Manufacturing, Cranfield University, Bedford, U.K.

He was an Engineer with Gansu Special Equipment Inspection & Testing Research Institute, Lanzhou, China, for six years. His current research interests include nondestructive testing (NDT) methods, especially miniaturized NDT techniques for *in situ* inspection.

Yifan Zhao was born in Zhejiang, China. He received the Ph.D. degree in automatic control and system engineering from the University of Sheffield, Sheffield, U.K., in 2007.

He is currently a Senior Lecturer in data science with Cranfield University, Bedford, U.K. His current research interests include computer vision, signal processing, nondestructive testing, active thermography, and nonlinear system identification.